Journal of the Chinese Institute of Engineers, 2015
Vol. 38, No. 5, 653–664, http://dx.doi.org/10.1080/02533839.2015.1009410

Direct georeferencing of airborne pushbroom images

Ching-Kuo Yeh and Victor J.D. Tsai*

Department of Civil Engineering, National Chung Hsing University, 250 Kuokuang Road, Taichung 402, Taiwan

(*Received 8 March 2012; accepted 30 March 2014*)

Direct georeferencing (DG) for orthoimage production based on collinearity equations has emerging as a standard photogrammetric operation. In this paper, the basic idea of DG is realized and refined with 19 self-calibration parameters for rectifying airborne pushbroom hyperspectral images collected using the intelligent spectral imaging system (ISIS) scanner. Two experimental ISIS images along with in-flight global positioning systems (GPS)/inertia measurement unit (IMU) data and 40 ground control points (GCPs) were used to solve these parameters by the iterative least squares method. By applying the proposed self-calibrated DG approach, the positional error of the GCPs is dramatically reduced to the pixel level from the 10-pixel level of in-flight DG-based rectification without self-calibration. Similar results were also found for the 30 check points, whose coordinates were either measured by GPS Real-Time Kinematic, or interpolated from 5-m to 20-m digital elevation model data, even when the six lens distortion parameters were omitted. It is demonstrated that the proposed self-calibrated DG approach promisingly improves the quality of georeferencing results by reducing the geometric distortions caused by instability of the platform, including misalignments in GPS/IMU, stabilizer effects on aircraft vibration and rotation, interior parameters of the sensor's optical system, and variations in topography.

Keywords: direct georeferencing; hyperspectral scanner; orthoimage rectification; remote sensing

1. Introduction

Due to emerging developments in sensor and imaging technology in recent years, hyperspectral imaging has become a promising technique in remote sensing and has played important roles in land resource monitoring applications. In comparison with satellite-based sensors, airborne hyperspectral sensors have the advantages of high spectral resolution and mobility in image acquisition. Airborne hyperspectral sensor acquisition can provide a wealth of spectral variations of the ground surface within tiny spectral bandwidth. Such detailed spectral information makes accurate image interpretation and classification possible for agricultural management, resource investigation, disaster assessment, atmosphere science, and military uses. Thus, airborne hyperspectral imaging has gained increasing attention for its potential in sustainable development in resource-related applications.

In comparison with satellite images, airborne pushbroom images are always accompanied by violent geometric distortions because of the instability of the platform and large field of view of the linear array sensor (Wang et al. 2006). The generation of orthoimages from airborne pushbroom images requires accurate position and attitude information of every scan line collected and interpolated from global positioning systems (GPS) and inertia measurement unit (IMU) devices by applying direct georeferencing (DG) computations (Cariou and Chehdi 2008; Müller et al. 2002; Rizaldy and Firdaus 2012; Schroth 2004). Digital elevation model (DEM) data are usually necessary in such rectification for determining the scaling factor from image plane to the terrain and removing the effects caused by topographic relief displacement. The DEM resolution has to be chosen in respect to the designated ground resolution of the orthoimages. The higher the resolution of the DEM grid, the more accurate the DG-corrected images which result from backward resampling. If DEM data are not used, a virtual reference plane with average elevation of the interest area should be used instead in the computations. However, the questions of reliability, prediction of accuracy, and quality control in DG-based applications are still open and demand solutions (Schroth 2004).

This paper hereinafter describes the configuration of the airborne pushbroom intelligent spectral imaging system (ISIS) scanner, the principles and mathematical model of self-calibrated DG, experimental results from rectification of two test ISIS images, and conclusions.

2. Configuration of the airborne ISIS scanner

The airborne ISIS scanner was manufactured in 2004 by the Instrument Technology Research Center (ITRC), National Applied Research Laboratories and partially supported by the National Chung Hsing University in

*Corresponding author. Email: jdtsai@nchu.edu.tw

Table 1. Optical and spectral characteristics of the ISIS scanner.

Sensor	Atmel-T20 CCD
Number of pixels/line	1150
Number of spectral bands	218
Range of spectrum	427.2–945.7 nm
Bandwidth	5 nm at 450 nm 3 nm at 600 nm 3 nm at 900 nm
Imaging speed	30 frames/s
Dynamic range	12 bits
Field of view (FOV)	58.6°
Instantaneous field of view (IFOV)	0.00096 radians
Focal length (f)	0.019 m
Offset of PPS (x_0, y_0) from line center	(0.000, 0.000) m

Taiwan (Huang 2006). Table 1 shows the optical and spectral characteristics of the ISIS scanner in which the Atmel-T20 frame charge coupled device (CCD) sensor is organized in one dimension as a 218 channel spectral field in a spectral range of 427.2–945.7 nm and in the other dimension as an 1150 pixel spatial field, each with 12-bit dynamic range, for a scan line. The camera lens and spectrograph system of the ISIS scanner were carefully calibrated by the Electro-Optics Lab, ITRC for focal length, image distortion and spectrum curvature, irradiance vs. incidence angle, and GRISM (grating and prism) diffraction efficiency (Huang 2006).

As shown in Figure 1, the ISIS scanner and the IMU device were mounted in a ZEISS T-AS stabilizer onboard a Britten-Norman BN-2A Islander aircraft for mission flights. A Novatel GPS receiver antenna was precisely mounted vertically above the scanner on top of the BN-2A aircraft with the offset components carefully determined by intersection using two Trimble 603 total stations (Tsai, Kao, and Chen 2006). Meanwhile, an IGI AeroControl CCNS4 (Computer Controlled Navigation System, 4th generation) was also installed on board for aerial navigation and management in recording the time of exposure for GPS control with a Leica MC500 GPS receiver. During the scanning mission, a Leica SR530 GPS receiver located at a fixed ground base station operated at the same epochs as that of the on-board Leica MC500 receiver. The system also incorporates an Applanix POS AV510, which integrates and synchronizes the measurements from both GPS and IMU devices for capturing in-flight position and attitude data in order to interpolate the exterior orientation parameters of the exposure center of every scan line by differential GPS technique.

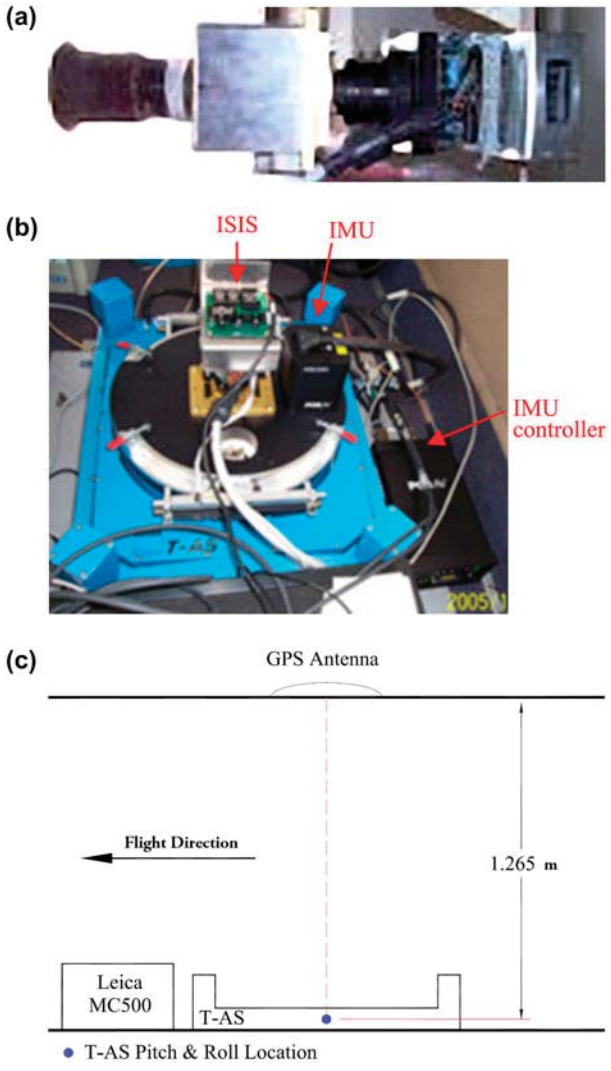

Figure 1. The integrated airborne pushbroom ISIS hyperspectral scanner: (a) the ISIS scanner (courtesy ITRC); (b) ISIS and IMU on a T-AS stabilizer; (c) offsets of GPS antenna vs. T-AS center on the BN-2A Islander aircraft.

3. Principles of DG with self-calibration

DG with the use of GPS/IMU devices has rapidly developed in recent decades and is nowadays standard in photogrammetry for high-accuracy mapping (Rizaldy and Firdaus 2012; Schroth 2004). Many studies applying DG have been published. Some of the areas where it has been applied are: photogrammetric aerial triangulation (AT) (Cramer 2001; Mostafa 2001a), system calibration to solve linear drift in positions and attitudes (Cramer and Stallmann 2002; Liu et al. 2011; Mostafa 2001b), sensor position and attitude modeling with polynomial function (Poli 2001), error budget analysis of airborne frame imagery (Mostafa, Hutton, and Lithopoulos 2001), performance assessments of large format digital cameras (Qtaishat 2011), estimation of unknown or inaccurate flight attitude parameters (Cariou and Chehdi 2008), orthoimage production from airborne and spaceborne line scanner images (Müller et al. 2002), and UAV platforms

(Bláha et al. 2011; Chiang, Tsai, and Chu 2012; Pfeifer, Glira, and Briese 2012).

As shown in Figure 2, the DG approach for orthoimage production using line scanner imagery usually implements three-dimensional (3-D) conformal transformations among the coordinate systems defined by the imaging sensor, GPS antenna, IMU, and object space, respectively, based on the collinearity concept (Cariou and Chehdi 2008; Cramer 2001; Mostafa 2001b; Müller et al. 2002; Schroth 2004):

$$\boldsymbol{V}_{\boldsymbol{O-P}}^{\boldsymbol{Obj}} = \boldsymbol{V}_{\boldsymbol{O-S}}^{\boldsymbol{Obj}} + \boldsymbol{V}_{\boldsymbol{S-P}}^{\boldsymbol{Obj}}, \tag{1}$$

in which $\boldsymbol{V}_{\boldsymbol{O-P}}^{\boldsymbol{Obj}} = \begin{bmatrix} X_P^{Obj} \\ Y_P^{Obj} \\ Z_P^{Obj} \end{bmatrix}$ is the vector from the origin to the target point $\boldsymbol{P}$ in object space,

$\boldsymbol{V}_{\boldsymbol{O-S}}^{\boldsymbol{Obj}} = \begin{bmatrix} X_S^{Obj} \\ Y_S^{Obj} \\ Z_S^{Obj} \end{bmatrix} = \boldsymbol{V}_{\boldsymbol{O-GPS}}^{\boldsymbol{Obj}} + \boldsymbol{R}_{\boldsymbol{O-S}}^{\boldsymbol{Obj}} \cdot \boldsymbol{V}_{\boldsymbol{GPS-S}}^{\boldsymbol{Obj}}$ is the vector from the origin to the sensor's exposure center in object space,

$\boldsymbol{V}_{\boldsymbol{S-P}}^{\boldsymbol{Obj}} = S_G \cdot \boldsymbol{R}_{\boldsymbol{O-S}}^{\boldsymbol{Obj}} \cdot \boldsymbol{V}_{\boldsymbol{S-p}}^{\boldsymbol{Prj}}$ is the vector from the sensor's exposure center to the target point $\boldsymbol{P}$ in object space, and

S_G is the scale factor from $\boldsymbol{V}_{\boldsymbol{S-p}}^{\boldsymbol{Prj}}$ in image frame to $\boldsymbol{V}_{\boldsymbol{S-P}}^{\boldsymbol{Obj}}$ in object space, i.e. $S_G = \dfrac{\boldsymbol{V}_{\boldsymbol{S-P}}^{\boldsymbol{Obj}}}{\boldsymbol{V}_{\boldsymbol{S-p}}^{\boldsymbol{Prj}}}$,

$\boldsymbol{R}_{\boldsymbol{O-S}}^{\boldsymbol{Obj}}$ is the rotating matrix between image frame and object space,

$\boldsymbol{V}_{\boldsymbol{S-p}}^{\boldsymbol{Prj}} = \begin{bmatrix} x_p \\ y_p \\ -f \end{bmatrix}$ is the vector from the sensor's exposure center to pixel $\boldsymbol{p}$ in image frame,

$\boldsymbol{V}_{\boldsymbol{O-GPS}}^{\boldsymbol{Obj}} = \begin{bmatrix} X_{GPS}^{Obj} \\ Y_{GPS}^{Obj} \\ Z_{GPS}^{Obj} \end{bmatrix}$ is the recorded position vector of the GPS antenna in object space,

$\boldsymbol{V}_{\boldsymbol{GPS-S}}^{\boldsymbol{Obj}} = \begin{bmatrix} X_{la}^{Obj} \\ Y_{la}^{Obj} \\ Z_{la}^{Obj} \end{bmatrix}$ is the fixed lever arm offsets of the GPS antenna to the center of the sensor.

Hence, Equation (1) can be rewritten as:

$$\begin{aligned} \boldsymbol{V}_{\boldsymbol{O-P}}^{\boldsymbol{Obj}} &= \boldsymbol{V}_{\boldsymbol{O-GPS}}^{\boldsymbol{Obj}} + \boldsymbol{R}_{\boldsymbol{O-S}}^{\boldsymbol{Obj}} \cdot \boldsymbol{V}_{\boldsymbol{GPS-S}}^{\boldsymbol{Obj}} + S_G \cdot \boldsymbol{R}_{\boldsymbol{O-S}}^{\boldsymbol{Obj}} \cdot \boldsymbol{V}_{\boldsymbol{S-p}}^{\boldsymbol{Prj}} \\ &= \boldsymbol{V}_{\boldsymbol{O-GPS}}^{\boldsymbol{Obj}} + \boldsymbol{R}_{\boldsymbol{O-S}}^{\boldsymbol{Obj}} \left(\boldsymbol{V}_{\boldsymbol{GPS-S}}^{\boldsymbol{Obj}} + S_G \cdot \boldsymbol{V}_{\boldsymbol{S-p}}^{\boldsymbol{Prj}} \right), \end{aligned} \tag{2}$$

in which $\boldsymbol{R}_{\boldsymbol{O-S}}^{\boldsymbol{Obj}} = \begin{bmatrix} \cos\kappa' & \sin\kappa' & 0 \\ -\sin\kappa' & \cos\kappa' & 0 \\ 0 & 0 & 1 \end{bmatrix} \begin{bmatrix} \cos\phi' & 0 & -\sin\phi' \\ 0 & 1 & 0 \\ \sin\phi' & 0 & cos\phi' \end{bmatrix} \begin{bmatrix} 1 & 0 & 0 \\ 0 & \cos\omega' & \sin\omega' \\ 0 & -\sin\omega' & \cos\omega' \end{bmatrix}$,

with $\omega' = S_\omega \cdot \omega + \omega_0$, $\phi' = S_\phi \cdot \phi + \phi_0$, and $\kappa' = S_\kappa \cdot \kappa + \kappa_0$ where $(S_\omega, S_\phi, S_\kappa)$ are the scaling factors of the T-AS stabilizer against sensor's attitude angles, (ω, ϕ, κ) are the attitude angles of the sensor, and

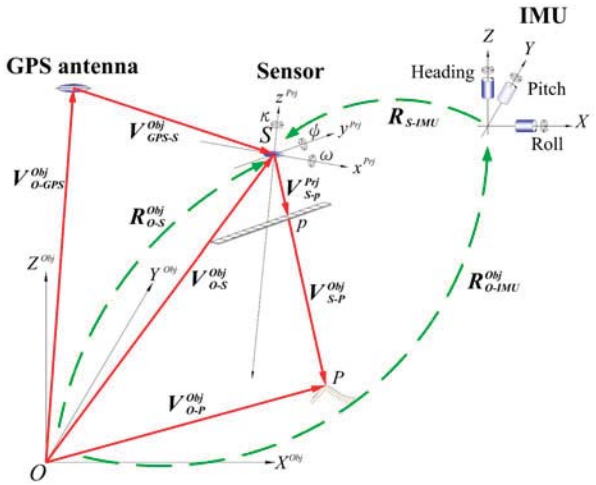

Figure 2. Concept of DG-based orthoimage production using linear scanner image.

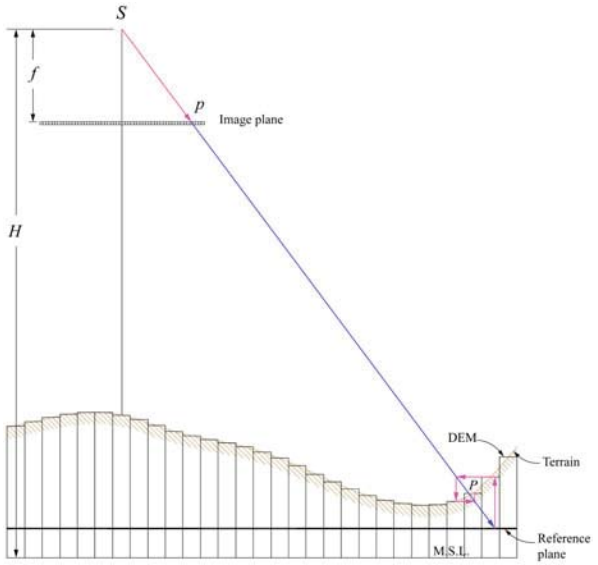

Figure 3. Determination of the scale factor S_G from DEM surface.

Table 2. Metadata of the experimental ISIS images.

Strip ID	07051501	08092901	
		08092901-1	08092901-2
Date scanned	15 May 2007	29 September 2008	
Number of scan lines	1500	2800	2633
Scan duration	46.94426 s	170.11407 s	
Average time lap between line	0.031317 s	0.031317 s	
GPS epochs	0.1 s	0.1 s	
Length of strip	2672.237 m	9895.144 m	
Minimum flying height (H_{min})[a]	1980.150 m	1129.987 m	
Average flying height (H_{avg})[a]	1988.573 m	1209.200 m	
Maximum flying height (H_{max})[a]	1999.061 m	1241.278 m	
Ground resolution on H_{min}	1.90 m	1.08 m	

[a]WGS84 Ellipsoid height of on-board GPS antenna.

$(\omega_0, \phi_0, \kappa_0)$ are the boresight misalignment angles of the IMU.

However, there exist several factors which affect the geometry of the raw data and limit the overall accuracy in DG-based orthoimage production (Cramer and Stallmann 2002; Honkavaara et al. 2006; Mostafa 2001b; Mostafa, Hutton, and Lithopoulos 2001; Müller et al. 2002; Qtaishat 2011; Zhao et al. 2013). These factors include the interior and exterior orientation parameters of the sensor's optical system, boresight angles between the IMU sensor and ISIS scanner, lever-arm offsets between the GPS receiver and ISIS scanner, scaling factors of the T-AS stabilizer that reduce the vibration and rotation of the aircraft in flight, and the topography of the earth surface. Hence, many quality control procedures have been applied by refining a mathematical model with high redundancy and reliability of an indirect method like AT (Cramer 2001; Mostafa, Hutton, and Lithopoulos 2001; Qtaishat 2011; Schroth 2004). The topic of self-calibration is of special concern when GPS/IMU components are used as one essential part of an airborne sensor system (Bäumker and Heimes 2002; Poli 2001).

This paper develops a self-calibrated DG approach for rectifying airborne pushbroom ISIS hyperspectral images with in-flight GPS/IMU data. The proposed self-calibrated DG approach adopts 19 additional parameters for correcting the geometric distortions caused by drifts or errors in the following parameters (Honkavaara 2004; Honkavaara et al. 2006; Liu et al. 2011):

(1) GPS receiver lever-arm offsets: for the ISIS installation as shown in Figure 1 with precise measurement from GPS antenna to T-AS stabilizer (Tsai, Kao, and Chen 2006), let (X_{la}, Y_{la}, Z_{la}) represent the offsets from the exposure center of the ISIS senor to the center of the T-AS stabilizer, thus

$$\boldsymbol{V}_{\boldsymbol{GPS-S}}^{\boldsymbol{Obj}} = \begin{bmatrix} X_{la}^{Obj} \\ Y_{la}^{Obj} \\ Z_{la}^{Obj} \end{bmatrix} = \begin{bmatrix} X_{la} \\ Y_{la} \\ Z_{la} + 1.265 \end{bmatrix}, \tag{3}$$

(2) IMU boresight misalignment angles $(\omega_0, \phi_0, \kappa_0)$;
(3) T-AS stabilizer scaling factors (S_ω, S_ϕ, S_κ) over the vibration and rotation of the aircraft: combining together with IMU boresight misalignment angles in Equation (2) for the refined attitude parameters $(\omega', \phi', \kappa')$ in a linear relation as:

$$\begin{cases} \omega' = S_\omega \cdot \omega + \omega_0 \\ \phi' = S_\phi \cdot \phi + \phi_0 \\ \kappa' = S_\kappa \cdot \kappa + \kappa_0 \end{cases}, \tag{4}$$

(4) Variation of the sensor's CCD size in column direction (δ_c); and
(5) Interior orientation parameters of the sensor's optical system, including focal length (f) and offsets of the principal point (x_0, y_0), and the radial and de-centering lens distortions (K_0, K_1, K_2, K_3, P_1, P_2) as in Equation (5) (Brown 1971):

$$\begin{cases} \Delta x = x_p(K_0 + K_1 r^2 + K_2 r^4 + K_3 r^6) + \left[P_1\left(r^2 + 2{x_p}^2\right) + 2P_2 x_p y_p\right] \\ \Delta y = y_p(K_0 + K_1 r^2 + K_2 r^4 + K_3 r^6) + \left[2P_1 x_p y_p + P_2\left(r^2 + 2{y_p}^2\right)\right] \end{cases}, \tag{5}$$

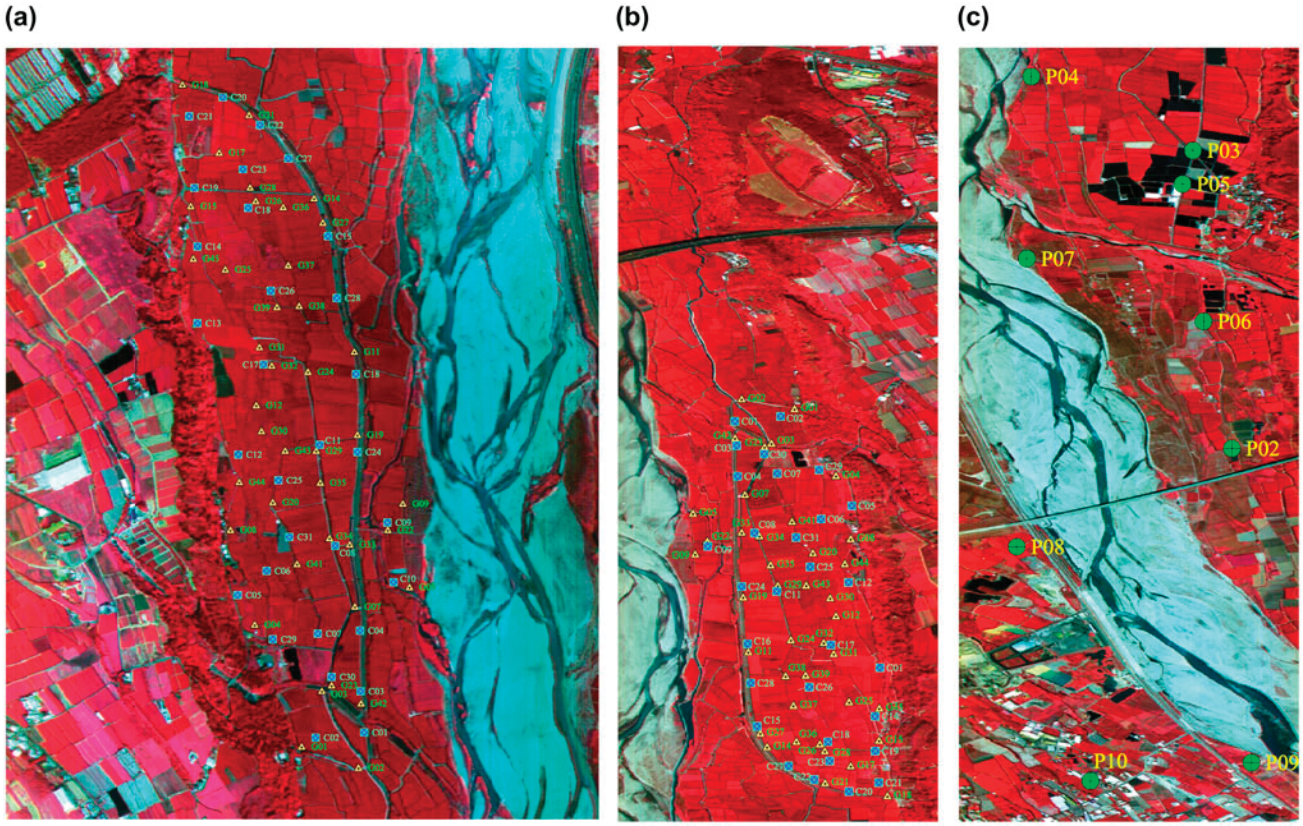

Figure 4. Raw ISIS images in NIR color composite (Red: λ_{182} = 869.9 nm, Green: λ_{94} = 654.6 nm, Blue: λ_{52} = 551.9 nm) with distribution of GCPs (*G*'s; △), CkPs (*C*'s; ▣) and ICPs (*P*'s; ●): (a) 07051501; (b) 08092901-1 (lines: 1–2800); (c) 08092901-2 (lines: 2801–5433).

in which $x_p = -x_0$, $y_p = 0.00096 \cdot f \cdot \delta_c \cdot (c_p - 575) - y_0$, and $r = \sqrt{x_p^2 + y_p^2}$ for a pixel $\boldsymbol{p}$ at column c_p of a scan line in the ISIS image. Thus, with corrections for lens distortions, the vector from the exposure center of sensor to pixel $\boldsymbol{p}$ in a scan line in Equation (2) is rewritten as:

$$\boldsymbol{V}_{S-p}^{Prj} = \begin{bmatrix} x_p + \Delta x \\ y_p + \Delta y \\ z_p \end{bmatrix} = \begin{bmatrix} -x_0 + \Delta x \\ 0.00096 \cdot f \cdot \delta_c \cdot (c_p - 575) - y_0 + \Delta y \\ -f \end{bmatrix}. \quad (6)$$

These 19 additional parameters for self-calibration were determined in a least squares solution of the linearized observation equations of Equation (3) formed using a series of well-distributed ground control points (GCPs) whose coordinates in object space were precisely measured. Meanwhile, DEM data describing the topographic surface in the same object space are required in determining the scale factor S_G from $\boldsymbol{V}_{S-p}^{Prj}$ to $\boldsymbol{V}_{S-P}^{Obj}$ as in Equation (2) in an iterative process from a given reference plane (Müller et al. 2002) as shown in Figure 3. Then, the bilinear interpolation resampling technique was applied for obtaining the rectified image pixel values.

4. Experimental results

As shown in Table 2, two strips of raw ISIS images: (a) 07051501 acquired on 15 May 2007 with 1.90 m ground resolution, and (b) 08092901 acquired on 29 September 2008 with 1.08 m ground resolution, covering the north bank of the Tachia River in Waipu District, Taichung City, Taiwan, were used in the experiment. The raw ISIS images were stored in 12-bit band-interleaved by line ENVI standard format along with a POS GPS-IMU text file for the exterior orientation data of every scan line, as provided by ITRC. It should be noted that the attitude angles (ω, ϕ, κ) of the ISIS scanner were recorded by the on-board POS as (*roll*, *pitch*, *heading*) of the IMU with $\omega = -roll$, $\phi = pitch$, $\kappa = heading - 90°$. The exterior orientation parameters for each scan line were processed and interpolated from original GPS/IMU observations by ITRC using Applanix POS AV510 post-processing software (Huang 2006) with in-flight

Table 3. Solved calibration parameters for ISIS images.

Additional parameter	Strip ID	
	07051501	08092901-1
X_{la}	-0.0024 ± 0.304 m	-0.0153 ± 0.304 m
Y_{la}	-0.1307 ± 0.304 m	-0.0700 ± 0.304 m
Z_{la}	0.0497 ± 0.304 m	0.1240 ± 0.304 m
ω_0	$0.0094 \pm 1.779 \times 10^{-2}$ rad	$0.0106 \pm 3.653 \times 10^{-2}$ rad
ϕ_0	$0.0120 \pm 3.742 \times 10^{-3}$ rad	$0.0121 \pm 8.882 \times 10^{-3}$ rad
κ_0	$0.0153 \pm 2.401 \times 10^{-4}$ rad	$-0.0002 \pm 2.779 \times 10^{-4}$ rad
S_ω	$1.0065 \pm 2.046 \times 10^{-4}$	$1.0013 \pm 3.893 \times 10^{-4}$
S_ϕ	$1.0000 \pm 9.697 \times 10^{-4}$	$1.0176 \pm 2.895 \times 10^{-4}$
S_κ	$0.9992 \pm 2.193 \times 10^{-3}$	$1.0216 \pm 1.653 \times 10^{-4}$
δ_c	$1.0000 \pm 1.902 \times 10^{-3}$	$1.0000 \pm 1.532 \times 10^{-3}$
f	$0.0190 \pm 3.875 \times 10^{-6}$ m	$0.0190 \pm 5.239 \times 10^{-6}$ m
x_0	$1.523 \times 10^{-8} \pm 3.88 \times 10^{-6}$ m	$9.499 \times 10^{-8} \pm 5.24 \times 10^{-6}$ m
y_0	$-0.723 \times 10^{-8} \pm 3.88 \times 10^{-6}$ m	$-1.174 \times 10^{-8} \pm 5.24 \times 10^{-6}$ m
K_0	$2.7980 \times 10^{-5} \pm 0.95 \times 10^{-5}$	$1.1909 \times 10^{-5} \pm 0.72 \times 10^{-5}$
K_1	$-1.0195 \times 10^{-5} \pm 0.40 \times 10^{-5}$	$-1.4255 \times 10^{-5} \pm 0.11 \times 10^{-5}$
K_2	$9.9417 \times 10^{-7} \pm 4.64 \times 10^{-7}$	$6.8665 \times 10^{-8} \pm 4.63 \times 10^{-8}$
K_3	$-2.8630 \times 10^{-8} \pm 1.56 \times 10^{-8}$	$-8.1562 \times 10^{-10} \pm 5.58 \times 10^{-10}$
P_1	$2.9334 \times 10^{-13} \pm 6.00 \times 10^{-13}$	$-3.2880 \times 10^{-13} \pm 2.99 \times 10^{-13}$
P_2	$-8.3500 \times 10^{-13} \pm 7.91 \times 10^{-13}$	$-3.8725 \times 10^{-13} \pm 4.27 \times 10^{-13}$
σ_0^*	2.413 m (1.27 pixels)	1.924 m (1.78 pixels)

*Standard error of unit weight.

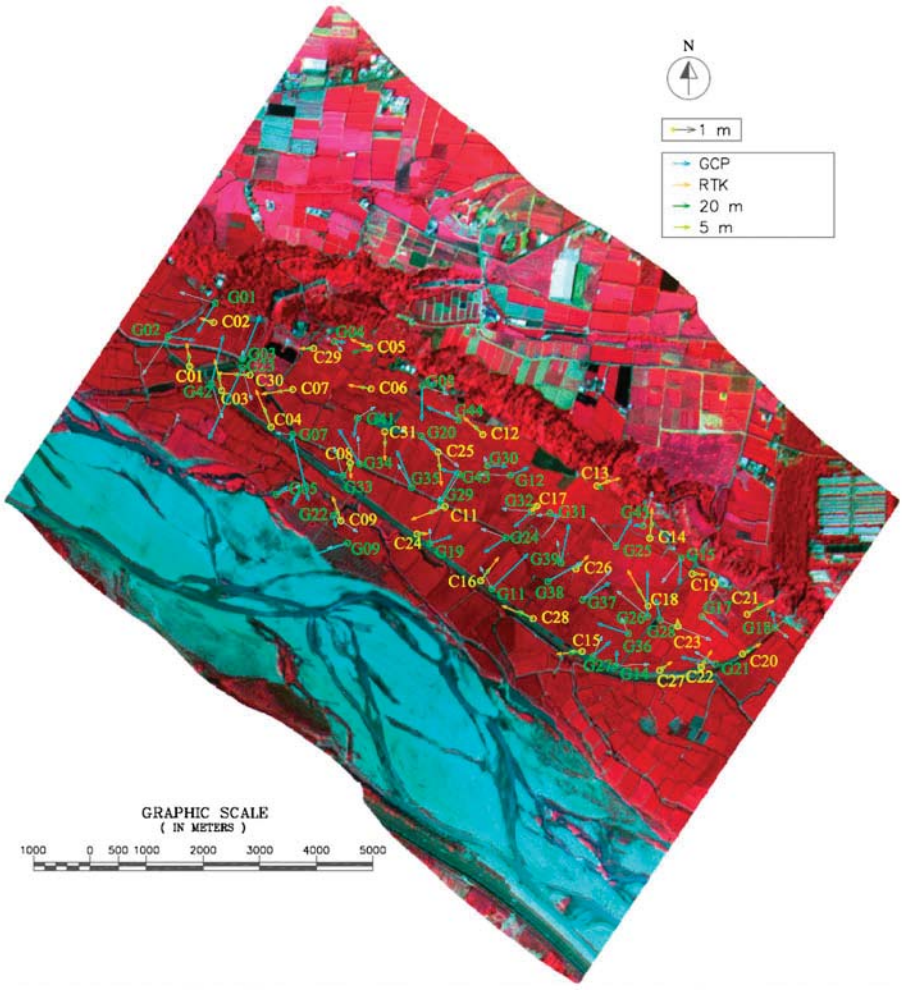

Figure 5. Rectified image 07051501 NIR color composite with error vectors of GCPs (*G*'s) and CkPs (*C*'s) from the proposed DG-19 approach.

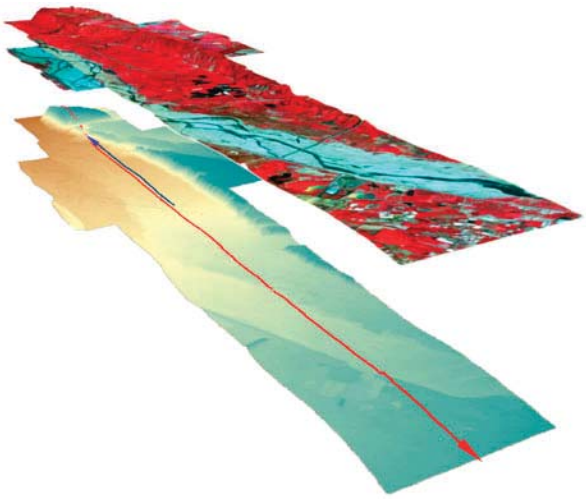

Figure 6. 3-D view of the rectified 07051501 image (3478 lines × 3172 pixels) and 08092901 image (7113 lines × 8024 pixels) in NIR color composite draped on top of 5-m DEM.

boresight calibration. The raw images of the two strips in near-infrared (NIR) color composite (Red: λ_{182} = 869.9 nm, Green: λ_{94} = 654.6 nm, Blue: λ_{52} = 551.9 nm) are shown in Figure 4 in row-wise order with the distribution of 40 GCPs (*G*'s in △) and 30 ground check points (CkPs; *C*'s in ▣). Note that strip 08092901 was used for solving self-calibration parameters with control points in the first 2800 lines of the strip (08092901-1), and for validation of self-calibrated DG the remaining 2633 lines of the strip (08092901-2) with 10 image check points (ICPs; *P*'s in ⊕) were selected from 1/5000 orthoimage with 50-cm resolution.

The ground coordinates of the 40 GCPs and 30 CkPs were surveyed using the GPS Real-Time Kinematic (GPS-RTK) approach with accuracies of 0.02 m in horizontal and 0.05 m in vertical direction. The 40 GCPs along with the ITRC-provided Applanix POS GPS/IMU data for every scan line of the raw ISIS images were used to solve for the 19 self-calibration parameters in DG (named the DG-19 approach) by least squares approach with equal weights. As shown in Table 3, the standard errors of unit weight (σ_0) are 2.413 and 1.924 m for the 07051501 and 08092901-1 strips, respectively. The parameters for interior orientation of the ISIS scanner, i.e. $f = 0.019$ m and $(x_0, y_0) = (0.000, 0.000)$, agree with its calibration results from the Electro-Optical Lab of ITRC as shown in Table 1. The parameters of strip 08092901-1 were also verified in rectifying the 08092901-2 strip.

Figure 5 shows the rectified 07051501 image in 1-m-ground resolution by the proposed DG-19 approach with 5-m DEM data for terrain interpolation in determining the scale factor S_G of each designated grid point on the terrain surface. The positional error vectors of the 40 GCPs and the 30 CkPs were graphically overlapped on the rectified image for comparison. Figure 6 shows a 3-D view of both rectified images in NIR color composite on the 5-m DEM surface for demonstrating the variation in topography. As shown in Table 4, the positional errors ($RMSE_{X-Y}$) of the 40 GCPs are significantly reduced to 2.949 and 2.583 m (pixel level) of the proposed self-calibrated DG-19 approach from 28.231 and 18.759 m (10-pixel level) of the in-flight DG approach for the two ISIS images, respectively. Similar results can also be found for the 30 CkPs, which were used to examine the reliability of solved self-calibration parameters in rectifying the ISIS images in topographic variations. By exploiting Equation (3), the resulting residuals primarily came from the in-flight POS-recorded position and attitude parameters which were interpolated every 0.031 s from a 0.1 s epoch of GPS receiver and synchronized IMU data.

Meanwhile, as shown in Table 3, the six parameters for the lens distortions of the optical system, i.e. $K_0 \sim K_3$ and $P_1 \sim P_2$, are in the area of 10^{-5} or less and are negligible for the ISIS scanner, so are not listed in the calibration parameters in Table 1 from ITRC. Thus, self-calibrated DG with 13 additional parameters (named the DG-13 approach) is feasible for the orthoimage production of the ISIS images by omitting Equation (5) and rewriting Equation (6) as the following with $(x_0, y_0) = (0.000, 0.000)$,

Table 4. Quality of self-calibrated DG with 19 parameters (DG-19) in the experimental ISIS images.

Points	Strip ID	Method	$RMSE_X$ (m)	$RMSE_Y$ (m)	$RMSE_{X-Y}$ (m)	$RMSE_H$ (m)
Ground control points (40 *G*'s)	07051501	In-flight DG	8.791	26.827	28.231	2.148
		Self-calibrated DG-19	1.742	2.379	2.949	2.450
	08092901-1	In-flight DG	5.614	17.899	18.759	2.800
		Self-calibrated DG-19	1.886	1.765	2.583	1.637
Ground check points (30 *C*'s)	07051501	20-m DEM DG-19	1.727	1.712	2.431	4.806
		5-m DEM DG-19	1.653	1.729	2.392	2.420
		GPS-RTK DG-19	1.656	1.662	2.347	2.218
	08092901-1	20-m DEM DG-19	1.661	2.034	2.626	5.909
		5-m DEM DG-19	1.764	2.096	2.740	3.277
		GPS-RTK DG-19	1.745	2.126	2.750	1.661

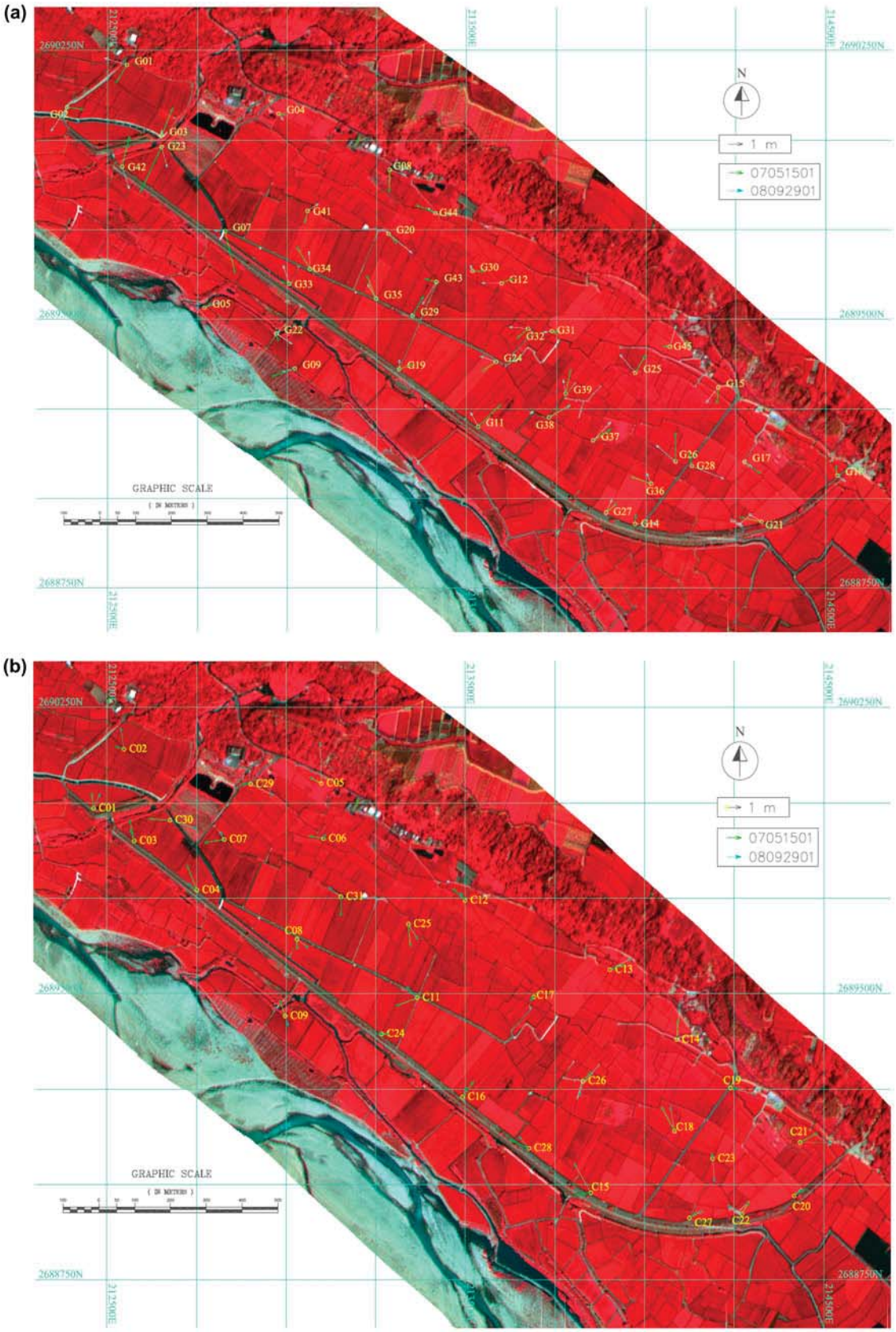

Figure 7. Positional error vectors from the DG-13 approach on rectified 08092901-1 image: (a) 40 GCPs (*G*'s) with ground coordinates from GPS-RTK; (b) 30 CkPs (*C*'s) with ground coordinates from GPS-RTK.

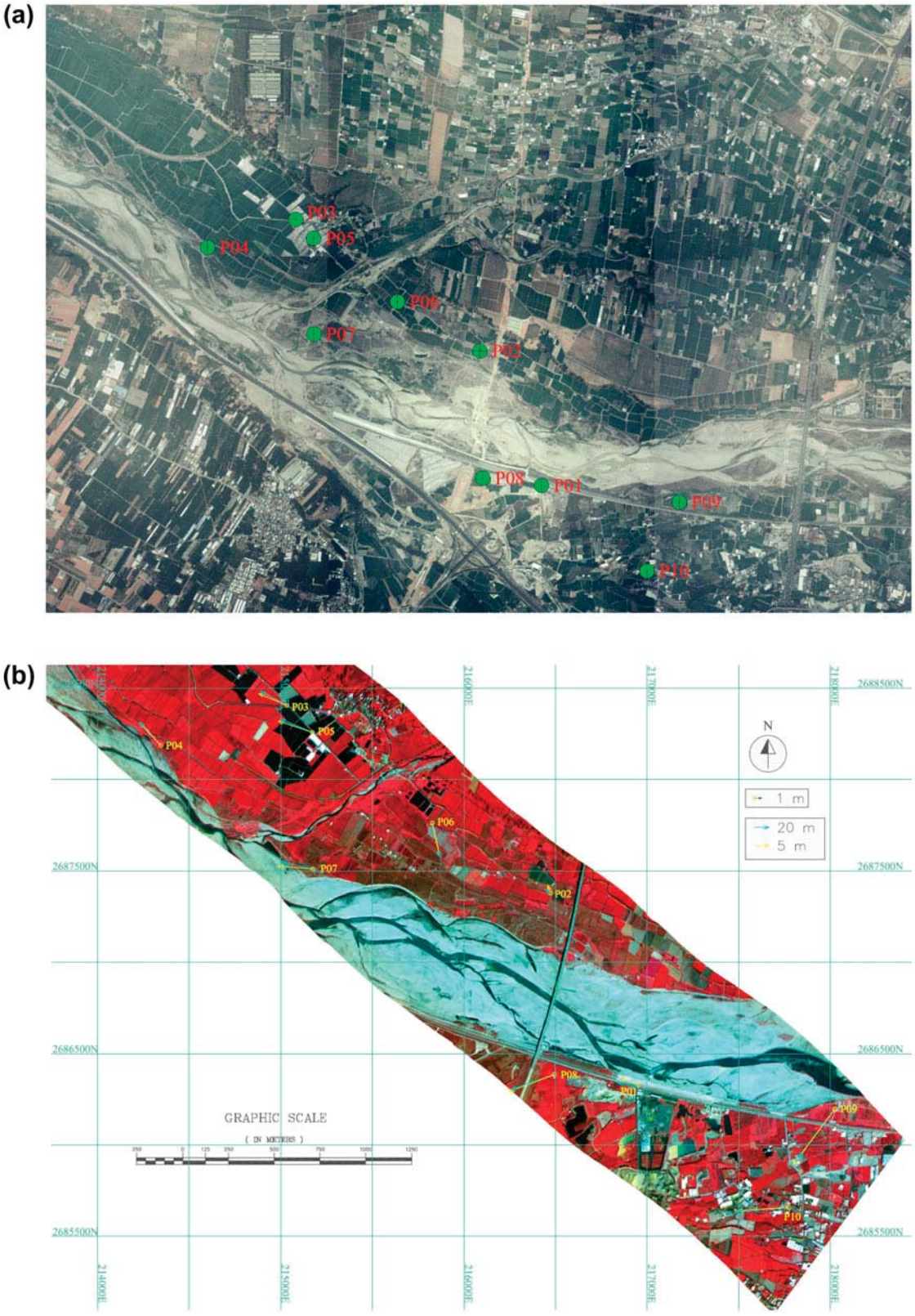

Figure 8. Image check points (ICPs; *P*'s) and their positional error vectors from the DG-13 approach: (a) 10 ICPs with plain coordinates from 1/5000 orthoimage; (b) Positional error vectors of the 10 ICPs on rectified 08092901-2 image.

Table 5. Quality of self-calibrated DG with 13 parameters (DG-13) in the experimental ISIS images.

Points	Strip ID	Method	$RMSE_X$ (m)	$RMSE_Y$ (m)	$RMSE_{X-Y}$ (m)	$RMSE_H$ (m)
Ground control points (40 *G*'s)	07051501	Self-calibrated DG-13	1.839	2.628	3.207	2.450
	08092901-1	Self-calibrated DG-13	2.097	2.105	2.971	1.638
Ground check points (30 *C*'s)	07051501	20-m DEM DG-13	1.673	1.723	2.401	4.809
		5-m DEM DG-13	1.609	1.738	2.368	2.427
		GPS-RTK DG-13	1.616	1.690	2.339	2.222
	08092901-1	20-m DEM DG-13	1.950	2.198	2.938	5.904
		5-m DEM DG-13	2.276	2.373	3.288	3.155
		GPS-RTK DG-13	2.257	2.438	3.322	2.876
Image check points (10 *P*'s)	08092901-2	20-m DEM DG-13	3.008	2.977	4.232	NA
		5-m DEM DG-13	4.413	3.209	5.457	NA

$$\boldsymbol{V}_{\boldsymbol{S-p}}^{\boldsymbol{Prj}} = \begin{bmatrix} x_p \\ y_p \\ z_p \end{bmatrix} = \begin{bmatrix} -x_0 \\ 0.00096 \cdot f \cdot \delta_c \cdot \left(c_p - 575\right) - y_0 \\ -f \end{bmatrix}. \tag{7}$$

The DG-13 approach was validated by examining the positional errors of the 40 GCPs and 30 CkPs in both 07051501 and 08092901-1 strips. Figure 7 shows the positional error vectors of the 40 GCPs (*G*'s) and 30 CkPs (*C*'s), whose ground coordinates from GPS-RTK, derived from the DG-13 approach on the rectified 08092901 image, respectively. As shown in Table 5, the positional errors ($RMSE_{X-Y}$) of the 40 GCPs from DG-13 are 3.207 and 2.971 m for the two strips, respectively. Similar results can also be found for the 30 CkPs in Table 5 with the same pixel level of positional errors as those from the DG-19 approach.

Furthermore, to validate the reliability of solved parameters for use in different strips in the same flight, 10 ICPs (*P*s) selected from 1/5000 orthoimage, as shown in Figure 8(a), were used in strip 08092901-2, which is a continuing line right after strip 08092901-1. As shown in Figure 8(b) and Table 5, the positional errors of the 10 ICPS are 4.232 and 5.457 m for the DG-13 approach with the elevation interpolated from 20-m to 5-m DEMs, respectively. They are about 1.5 times the errors in GCPs, but are also acceptable at pixel level. As a result, the solutions of self-calibration parameters are reliable for rectifying other strips of the ISIS images in the same flight.

5. Conclusions

DG for orthoimage production based on collinearity equations has emerged as a standard photogrammetric operation. The on-board GPS/IMU data provides a rough solution to the in-flight DG approach, which assumes the post-processed position and attitude data are correct with sufficient accuracy. However, there exist several factors which affect the imaging geometry of the raw images and limit the spatial accuracy of the DG-based orthoimage production.

In this paper, the basic idea of DG was refined mathematically by introducing 19 additional parameters for self-calibration (DG-19) of airborne ISIS images. These additional self-calibration parameters are solved by the least squares method with precisely surveyed GCPs along with in-flight GPS/IMU position and attitude data and DEM data. Two ISIS hyperspectral images in different flight, each along with in-flight Applanix POS GPS/IMU data, and 40 GCPs and 30 CkPs with precisely surveyed ground coordinates were used in solving and validating the solved self-calibration parameters, respectively. Experimental results show that the interior parameters of the optical system agree with those parameters provided from ITRC. By applying the proposed self-calibrated DG-19 approach, the positional $RMSE_{X-Y}$ of the 40 GCPs for the two strips were significantly reduced to 2.949 m/2.583 m (pixel level) from 28.231 m/18.759 m (10-pixel level) of the in-flight DG-based rectification, and there are also consistent with those of 30 CkPs, whose coordinates were either measured by GPS-RTK, or interpolated from 5-m to 20-m DEM data. Similar results with pixel-level geometric accuracy were also obtained from the DG-13 approach in which the six lens distortion parameters were omitted. Our proposed self-calibrated DG approach improves the quality of the georeferencing results in reducing the geometric distortions caused by the instability of the platform, including GPS lever-arm offsets, IMU boresight misalignments, and T-AS stabilizer's scaling effects on aircraft vibration and rotation. The resulting residuals may primarily come from the position and attitude parameters which were interpolated from synchronized GPS receiver and IMU data. To improve the quality in DG-based image registration, further research on the filtering and interpolation of in-flight GPS/IMU data for

determining the position and attitude parameters of every scan line and much accurate digital surface model data from airborne LiDAR or traditional photogrammetric compilation for determining the scale factor S_G of each image pixel to its object point are required.

Nomenclature

c_p	Column of a pixel $\boldsymbol{p}$ in the image
δ_c	Variation of the sensor's CCD size in column direction
f	Focal length of the imaging system
K_0, K_1, K_2, K_3	Parameters for radial lens distortion
P_1, P_2	Parameters for decentering lens distortion
r	Radial distance of a pixel in image frame
$\Delta x, \Delta y$	Corrections to the image coordinates caused by radial and decentering lens distortions
x_p, y_p	Coordinates of pixel p in image frame
x_0, y_0	Offsets of the principal point of the imaging system
σ_0	Standard error of unit weight
$RMSE_X$, $RMSE_Y$, $RMSE_H$	Root mean squared errors in X, Y, and H directions
$RMSE_{X-Y}$	Root mean squared error in the X–Y plane
$\boldsymbol{R}_{\boldsymbol{O-S}}^{\boldsymbol{Obj}}$	Rotation matrix of the sensor formed by attitude angles between image frame and object space
ω, ϕ, κ	Attitude angles of the imaging sensor
ω', ϕ', κ'	Corrected attitude angles
$\omega_0, \phi_0, \kappa_0$	Initial alignment (boresight misalignment) angles of the IMU
S_G	Scale factor from image plane to object space
$S_\omega, S_\phi, S_\kappa$	T-AS stabilizer scaling factors on attitude angles
$\boldsymbol{V}_{\boldsymbol{O-P}}^{\boldsymbol{Obj}}$	Position vector of the target point $\boldsymbol{P}$ in object space
$\boldsymbol{V}_{\boldsymbol{O-S}}^{\boldsymbol{Obj}}$	Position vector of the exposure center in object space
$\boldsymbol{V}_{\boldsymbol{S-P}}^{\boldsymbol{Obj}}$	Vector from the exposure center to the target point $\boldsymbol{P}$ in object space
$\boldsymbol{V}_{\boldsymbol{O-GPS}}^{\boldsymbol{Obj}}$	Position vector of the GPS antenna in object space
$\boldsymbol{V}_{\boldsymbol{GPS-S}}^{\boldsymbol{Obj}}$	Vector from the GPS antenna phase center to the exposure center
$\boldsymbol{V}_{\boldsymbol{S-p}}^{\boldsymbol{Prj}}$	Vector from the exposure center to a pixel $\boldsymbol{p}$ in image frame
$X_P^{Obj}, Y_P^{Obj}, Z_P^{Obj}$	Coordinates of the target point $\boldsymbol{P}$ in object space
$X_S^{Obj}, Y_S^{Obj}, Z_S^{Obj}$	Coordinates of the exposure center in object space
$X_{GPS}^{Obj}, Y_{GPS}^{Obj}, Z_{GPS}^{Obj}$	Coordinates of the GPS antenna in object space
$X_{la}^{Obj}, Y_{la}^{Obj}, Z_{la}^{Obj}$	Lever-arm offsets of the GPS antenna to the exposure center
X_{la}, Y_{la}, Z_{la}	Offsets from the ISIS exposure center to the center of the ZEISS T-AS stabilizer

Funding

The partial funding support from the Ministry of Science and Technology of Taiwan under Contract Grants NSC 99-2221-E-005-084 and NSC 100-2221-E-005-075-MY2 in improving the developed approach is gratefully acknowledged.

References

Bäumker, M., and F. J. Heimes. 2002. "New Calibration and Computing Method for Direct Georeferencing of Image and Scanner Data Using The Position and Angular Data of An Hybrid Inertial Navigation System." In *Integrated Sensor Orientation*, edited by C. Heipke, K. Jacobsen and H. Wegmann, 197–212. Frankfurt am Main: Bundesamt für Kartographie und Geodäsie.

Bláha, M., H. Eisenbeiss, D. Grimm, and P. Limpach. 2011. "Direct Georeferencing of UAVs." In *Proceedings of International Conference on Unmanned Aerial Vehicle in Geomatics (UAV-g 2011)*, Zurich, Switzerland, 14–16 September 2011: 38-1 (C22): 1–6. Hannover: ISPRS.

Brown, D. C. 1971. "Close-range Camera Calibration." In *Proceedings of ASP Symposium on Close-range Photogrammetry*, Urbana, IL, 27–29 January 1971: 855–866. Bethesda, MD: American Society of Photogrammetry (ASP).

Cariou, C., and K. Chehdi. 2008. "Automatic Georeferencing of Airborne Pushbroom Scanner Images with Missing Ancillary Data Using Mutual Information." *IEEE Transactions on Geoscience and Remote Sensing* 46 (5): 1290–1300. doi:10.1109/TGRS.2008.916206.

Chiang, K. W., M. L. Tsai, and C. H. Chu. 2012. "The Development of An UAV Borne Direct Georeferenced Photogrammetric Platform for Ground Control Point Free Applications." *Sensors* 12 (7): 9161–9180. doi:10.3390/s120709161.

Cramer, M. 2001. "On The Use of Direct Geo-referencing in Airborne Photogrammetry." In *Proceedings of The 3rd International Symposium on Mobile Mapping Technology*, Cairo, Egypt, 3–5 January 2001: 1–13. Calgary: University of Calgary.

Cramer, M., and D. Stallmann. 2002. "System Calibration for Direct Georeferencing." In *Proceedings of ISPRS Commission III Symposium on Photogrammetric Computer Vision*, Graz, Austria, 9–13 September 2002: 34 (A): 79–84. Hannover: ISPRS.

Honkavaara, E. 2004. "In-flight Camera Calibration for Direct Georeferencing." In *International Archives of Photogrammetry, Remote Sensing and Spatial Information Sciences,*

XX ISPRS Congress, Istanbul, Turkey, 12–23 July 2004: 35 (B1): 166–171. Hannover: ISPRS.

Honkavaara, E., E. Ahokas, J. Hyyppä, J. Jaakkola, H. Kaartinen, R. Kuittinen, L. Markelin, and K. Nurminen. 2006. "Geometric Test Field Calibration of Digital Photogrammetric Sensors." *ISPRS Journal of Photogrammetry and Remote Sensing* 60 (6): 387–399. doi:10.1016/j.isprsjprs.2006.04.003.

Huang, T. M. 2006. "The Development of Hyperspectral Scanner at ITRC." In *Proceedings of The 13th Symposium on Applications of Resource Satellite Data/17th Resource Satellite Data User Meeting*, Jhongli, Taiwan, 28 April 2006: 1–27 (PowerPoint presentation in Chinese). Jhongli, Taiwan: National Central University.

Liu, J., D. Wang, H. Wang, and Y. Fan. 2011. "A Rigorous Approach for IMU Boresight Misalignment Calibration." In *Proceedings of International Workshop on Multi-platform/Multi-sensor Remote Sensing and Mapping (M2RSM)*, Xiamen, China, 10–12 January 2011: 1–4. New York: IEEE.

Mostafa, M. M. R. 2001a. "Direct Georeferencing Column: An Introduction." *Photogrammetric Engineering & Remote Sensing* 67 (10): 1105–1109.

Mostafa, M. M. R. 2001b. "Boresight Calibration of Integrated Inertial/Camera Systems." In *Proceedings of International Symposium on Kinematic Systems in Geodesy, Geomatics and Navigation – KIS 2001*, Banff, Canada, 5–8 June 2001: 440–445. Calgary: University of Calgary.

Mostafa, M. M. R., J. Hutton, and E. Lithopoulos. 2001. "Airborne Direct Georeferencing of Frame Imagery: An Error Budget." In *Proceedings of The 3rd International Symposium on Mobile Mapping Technology*, Cairo, Egypt, 3–5 January 2001: 1–12. Calgary: University of Calgary.

Müller, R., M. Lehner, R. Müller, P. Reinartz, M. Schroeder, and B. Vollmer. 2002. "A Program for Direct Geo-referencing of Airborne and Spaceborne Line Scanner Images." In *Proceedings of International Archives of Photogrammetry and Remote Sensing, Commission I*, Denver, CO, 10–15 November 2002: 34 (1): 148–153. Hannover: ISPRS.

Pfeifer, N., P. Glira, and C. Briese. 2012. "Direct Georeferencing with on Board Navigation Components of Light Weight UAV Platforms." In *International Archives of the Photogrammetry, Remote Sensing and Spatial Information Sciences, XXII ISPRS Congress*, Melbourne, Australia, 25 August–1 September 2012: 34 (B7): 487–492. Hanover: ISPRS.

Poli, D. 2001. "Direct Georeferencing of Multi-line Images with A General Sensor Model." In *Proceedings of ISPRS Workshop on High Resolution Mapping from Space 2001*, Hanover, Germany, 19–21 September 2001: 1–8. Hanover: ISPRS.

Qtaishat, K. S. 2011. "Assessing the Performance of Different Direct-georeferencing with Large Format Digital Cameras." *Jordan Journal of Civil Engineering* 5 (4): 545–551.

Rizaldy, A., and W. Firdaus. 2012. "Direct Georeferencing: A New Standard in Photogrammetry for High Accuracy Mapping." In *Proceedings of International Archives of the Photogrammetry, Remote Sensing and Spatial Information Sciences, XXII ISPRS Congress*, Melbourne, Australia, 25 August–1 September 2012: 34 (B1): 5–9. Hanover: ISPRS.

Schroth, R. 2004. "Direct Geo-referencing in Practical Applications." In *Proceedings of ISPRS Workshop WG I/5 on Theory, Technology and Realities of Inertial/GPS Sensor Orientation*, Castelldefels, Spain, 23 September 2004: 1–8. Hanover: ISPRS.

Tsai, V. J. D., J. S. Kao, and C. N. Chen. 2006. "On GPS and GPS-RTK Assisted Aerotriangulation." In *Proceedings of ASPRS 2006 Annual Conference*, Reno, Nevada, 1–5 May 2006: 1–10. Bethesda, MD: ASPRS.

Wang, Z., Y. Ma, R. Shu, W. Xu, and L. Yu. 2006. "Geometric Correction of IR Imaging Spectral Image Based on IMU/GPS Navigation System." In *Proceedings of Joint 31st International Conference on Infrared Millimeter Waves and 14th International Conference on Teraherz Electronics (IRMMW-THz 2006)*, Shanghai, China, 18–22 September 2006: 590. New York: IEEE.

Zhao, H., B. Zhang, C. Wu, Z. Zuo, and Z. Chen. 2013. "Development of a Coordinate Transformation Method for Direct Georeferencing in Map Projection Frames." *ISPRS Journal of Photogrammetry and Remote Sensing* 77: 94–103. doi:10.1016/j.isprsjprs.2012.12.004.